Available online at www.sciencedirect.com
ScienceDirect
Trans. Nonferrous Met. Soc. China 31(2021) 1853−1867
Transactions of Nonferrous Metals Society of China
www.tnmsc.cn

Microstructural evolution and microsegregation in directional solidification of hypoeutectic Al−Cu alloy: A comparison between experimental data and numerical results obtained via phase-field model

Alexandre F. FERREIRA[1], Ivaldo L. FERREIRA[2], Rangel P. ALMEIDA[1], José A. CASTRO[1], Roberto C. SALES[1], Zilmar A. JUNIOR[1]

1. Graduate Program on Metallurgical Engineering, Federal Fluminense University, 27255-125, Volta Redonda, RJ, Brazil;
2. Federal University of Pará, College of Mechanical Engineering, 66075-110, Belém, PA, Brazil

Received 23 July 2020; accepted 2 March 2021

Abstract: The objective of the work is focused on predictions of microsegregation, solidification speed, dendritic arm spacings and dendrite morphology by phase-field model. The numerical results were compared with experimental data. The experimental values for cooling rates and effective partition coefficient were adopted during calculations. The results of microsegregation through phase-field model show excellent agreement with the experimental data. Such excellent agreement is because cooling rates, effective partition coefficient and back-diffusion of solute are considered in the model. For solidification speed, the calculation results show good agreement with the experimental data. Tertiary dendritic arm spacing calculated with phase-field model is compared with experimental data. The results show good agreement between them. The dendrite arm spacing varies with position because high cooling rates are responsible for the refinement effect on microstructure. Finally, two-dimensional simulation produced a dendrite that is similar to that found in the experiment.

Key words: hypoeutectic Al−Cu alloy; effective partition coefficient; dendritic arm spacing; microsegregation; phase-field model

1 Introduction

From seminal experimental studies on alloys solidification using unidirectional solidification process, dating back to the early 1980s, a collection of experimental works have stemmed ever since, in order to investigate the microstructural growth during the solidification process [1−5]. This technique allows the study of the solid phase growth and as-cast microstructures as a function of the thermal variables (cooling rate, thermal gradient and local solidification time) and solidification speed, making it a very attractive technique for investigations of solidification process of alloys with eutectic or near-eutectic composition [6−8].

The microstructure obtained during the solidification process of metal alloys is a key factor due to its effect on the as-cast material properties. In other words, microstructure from aluminum alloys can strongly influence the mechanical properties such as strength, toughness, hardness and corrosion resistance. Addition of Cu solute in aluminum alloys, in turn, leads to an increase in the fluidity and better tensile strength [2]. Not only the microstructural morphology itself as cells, dendrites, inclusions, intermetallics and porosity, but also the chemical arrangement (segregation) which induces

Corresponding author: Alexandre F. FERREIRA, E-mail: alexandrefurtado@id.uff.br
DOI: 10.1016/S1003-6326(21)65622-4

non-uniformity of mechanical properties can affect corrosion resistance [9−12].

The microsegregation is the inhomogeneous distribution of solutes at the scales of cells or dendrite spacings. Microsegregation cannot be avoided during solidification, since it is the result of the solubility difference between the liquid and solid phases. An understanding of the segregation way occurring during solidification process should be of great importance for properties of as-cast alloys and in designing post-casting processes.

The alloy considered in the present work (Al−Cu alloy) is one of the most important high-strength aluminium alloys. Al−Cu alloys have been employed extensively in the aircraft and military industries, in which materials are frequently subjected to elevated temperatures. The aluminium casting alloys, based on the Al−Cu system are widely used in the light-weight constructions and transport applications requiring a combination of high strength and ductility [13].

In the last decades, appreciable attention has been paid, to the modeling and simulation by the phase-field model of solidification process and related phenomena [14−16]. Many different modeling approaches have been proposed to that end. Some numerical works have focused on pure materials, whereas others took heed of alloys of manufacturing interest. One example is the numerical work proposed by FERREIRA et al [13], who applied the phase-field model to such problems. In Ref. [13], the authors used phase-field model to simulate the solidification process for pure material (nickel) and the numerical results were compared with solidification theory and experimental data reported.

Numerical results have been published pertaining to phase-field modeling focused on microsegregation in ternary alloys by WYNBLATT and LANDA [15] and FERREIRA and OLIVÉ [14]. On the other hand, some numerical works have been performed focused on microsegregation and microstructural evolution in multicomponent alloys [16,17]. Phase-field models are known to be very powerful in describing non-equilibrium dendritic evolution. These models are very efficient especially in numerical treatment because all governing equations are written in unified forms without distinguishing the interface from solid and liquid phases. Direct tracking of the solid/liquid interface is not needed during solidification process simulation. The computational domain is represented by a distribution of the single variable known as “phase-field variable”.

Results have been published with phase-field modeling and simulation for solidification in binary alloys by KIM et al [18]. In that work, the phase-field model presented by authors (KKS), appears to be equivalent to the model proposed by WHEELER et al [19] (WBM), but with a different approach of the free energy density at the interface. A relationship between the interface mobility of phase-field model and the interface kinetics coefficient was derived under a thin-interface limit condition. These results show that the effect of the finite phase-field mobility tends to decrease the composition in solid region, whereas the effect of finite interface thickness increases the solute composition in that region. The profiles of concentration across the interface were determined as a function of the solid/liquid interface velocity. Under low solidification velocities, the simulated results were in agreement with the exact solutions. As expected, the effective partition coefficient becomes close to 1 at high solidification velocities.

A phase-field model for rapid solidification was dealt with by WANG et al [20]. In that work, a mobility for non-equilibrium solute diffusion is introduced in phase-field model, in which long-range solute diffusion and short-range solute redistribution were considered. According to Ref. [20], the model is applicable to rapid solidification of binary concentrated alloys and can be extended further to multi-component alloy systems.

A local non-equilibrium diffusion model (LNDM) for rapid solidification of binary alloys has been reviewed by SOBOLEV [21] and then used to modify solute trapping models with different interface kinetics. The proposed LNDM takes into account the deviation from local equilibrium of a solute diffusion field in liquid region on the basis that the solutions to diffusion equations govern the solute concentration and solute flux in liquid. According to SOBOLEV [21], the liquid diffusion speed is a critical parameter in determination of effective partition coefficient. The velocity dependence of partition coefficients has been calculated for different types of solid/liquid interface kinetics under local non-equilibrium

diffusion conditions. The calculation obtained by SOBOLEV [21] shows that the local effective partition coefficients reduce to the equilibrium partition coefficient at very low interface velocities and differ substantially when high interface velocity is considered.

The manifestation of rapid solidification phenomena is the solute trapping, which corresponds to solute redistribution between solid and liquid regions and obviously increases the solute concentration in the solid region and reduces the segregation on the liquid side. The degree of solute trapping can be usually determined by the partition coefficient. In the present work, we adopted a phase-field model, which is based on KKS model. The KKS model is well-known and previously modified by FERREIRA and OLIVÉ [14]. The advantage for using the solute partition model proposed by BURTON et al [22], is due to fact that equilibrium partition coefficient considered in phase-field model, is easily replaced by the effective partition coefficient. It is in this general framework that the present work is developed, i.e., a numerical investigation by phase-field model with focus on solidification process in hypoeutectic Al−Cu alloy. The effect of the non-equilibrium solidification was incorporated by solidification speed (S_S) into an effective partition coefficient (k_{ef}) that has been calculated for a range of solidification speed from 0.4 to 1.1 mm/s. The solidification speed (S_S), tertiary dendrite arm spacing (λ_3) and microsegregation profiles predicted by phase-field model, using the new partition coefficient and cooling rate, were compared with experimental data from hypoeutectic Al−5.0wt.%Cu alloy.

2 Phase-field modeling

In phase-field models, the state of the domain is customarily represented by a distribution of the single variable known as the "phase-field variable", in this present work represented by ϕ. The value ϕ=1 is associated with solid phase, ϕ=0 corresponds to the liquid and ϕ between 0 and 1 indicates the solid/liquid interface.

For simulation of solidification microstructure in binary alloy, two governing equations are used: one for phase field itself, the other for Cu concentration. The equations can be written as defined in SALVINO et al [16] and KIM et al [18]:

$$\left(\frac{1}{M}\right)\left(\frac{\partial\phi}{\partial t}\right)=\nabla\cdot\varepsilon(\theta)^2\nabla\phi-wg'(\phi)+\frac{RT}{V_m}h'(\phi)\ln\frac{(1-c_S^{eq})(1-c_L)}{(1-c_L^{eq})(1-c_S)}+N \tag{1}$$

$$\frac{\partial c}{\partial t}=\nabla\left\{D(\phi)[(1-h(\phi))(1-c_L)c_L+h(\phi)(1-c_S)c_S]\nabla\ln\left(\frac{c_L}{1-c_L}\right)\right\} \tag{2}$$

where $\partial\phi/\partial t$ represents the evolution of the solid nucleus with time; $h(\phi)=\phi^2(3-2\phi)$; $g(\phi)=\phi^2(1-\phi)^2$; the subscripts "S" and "L" stand for solid and liquid, respectively; R is the mole gas constant; V_m is the molar volume; T is the temperature; M, w and $\varepsilon(\theta)$ are phase-field parameters, with θ being the angle between the direction of the phase-field gradient and the reference axis of the system; N stands for noise; $D(\phi)$ is the Cu diffusion coefficient; c_S and c_L are concentrations of the solid and liquid phases, respectively. These phase-field parameters are related to the interface energy (σ), whereas the interface width (2λ) is the distance where ϕ changes from 0.1 to 0.9. The parameter M is related to the kinetic coefficient (β). From FERREIRA and OLIVÉ [14], these parameters are obtained as

$$\sigma=\frac{\varepsilon\sqrt{w}}{3\sqrt{2}} \tag{3}$$

$$2\lambda=2.2\sqrt{2}\frac{\varepsilon}{\sqrt{w}} \tag{4}$$

$$\beta=\frac{V_m}{RT}\frac{m_e}{1-k_{ef}}\left[\frac{\sigma}{M\varepsilon^2}-\frac{\varepsilon}{D_i\sqrt{2w}}\xi(c_S^{eq},c_L^{eq})\right] \tag{5}$$

$$\xi(c_S^{eq},c_L^{eq})=\frac{RT}{V_m}(c_S^{eq},c_L^{eq})^2\cdot\int_0^1\frac{h(\phi)[1-h(\phi)]}{[1-h(\phi)]c_L^{eq}(1-c_L^{eq})+h(\phi)c_s^{eq}(1-c_s^{eq})}\frac{d\phi}{\phi(1-\phi)} \tag{6}$$

where ε is the coefficient of phase-field gradient energy term; D_i is the diffusion coefficient in the interface region; $d\phi$ is the differential of the variable ϕ; m_e is the slope of liquidus line, k_{ef} is the effective partition coefficient, which is calculated as a function of solidification speed ($k_{ef}=f(S_S)$). The kinetic coefficient, β, is defined to be the inverse of the linear kinetic coefficient, μ_k. Equations (1) and (2) were solved numerically by explicit finite-

difference and discretized on uniform grids. The anisotropy is introduced in the phase-field model as follows [14,17]:

$$\varepsilon(\theta)=\varepsilon\{1+\delta_{\varepsilon}[j(\theta-\theta_0)]\} \quad (7)$$

where δ_{ε} gauges the anisotropy. The value j controls the number of preferential growth directions. The orientation of the maximum anisotropy is determined by the θ_0 constant. Asymmetrical microstructures are obtained in the phase-field simulations by a noise term on the right-hand side of Eq. (1), a usual expression for this noise, as indicated by FERREIRA and OLIVÉ [14] is

$$N=16ar\phi^{2}(1-\phi)^{2} \quad (8)$$

with r is the random number between −1 and 1; a is the noise amplitude. The physical properties of the Al−Cu alloy used during the computations can be found in Refs. [19,20]. The parameters used in the phase-field simulations were calculated from physical properties of the Al−Cu alloy by Eqs. (3)−(6).

Simulations were carried out by imposing the following linear temperature profile:

$$T=T_0-\dot{T}t \quad (9)$$

where T_0 is the initial temperature; $\dot{T}$ represents the cooling rate; t is the solidification time.

3 Microsegregation analysis

Microsegregation during solidification is an extremely important phenomenon. It occurs over distances of the order of the cell or dendrite spacings and can lead to large variations in alloy or impurity composition between the solidification microstructure core (the first material to solidify) and the microstructure boundaries (the last material to solidify). As a result, phase equilibria and microstructures of the as-cast material can be considerably different from those of the base material of the same composition [21]. For example, secondary phases which are not present in the wrought material may be present in the rapid solidification, a non-uniform precipitate distribution may occur in precipitation-strengthened alloys, and the phases stability in different regions of the microstructure may vary. All these factors have a great effect on the final as-cast material.

Microsegregation in solidification process is usually discussed in terms of plane-front solidification models developed for casting. However, the solidification speed and cooling rate are considerably high in industrial practice, and the resulting solidification structures can be finer [22,23]. These have a significant effect on the degree of microsegregation. Alloy partitioning during solidification can be defined by the volume element shown in Fig. 1. Plane-front solidification models can be described in this volume element to predict a variety of microsegregation profiles.

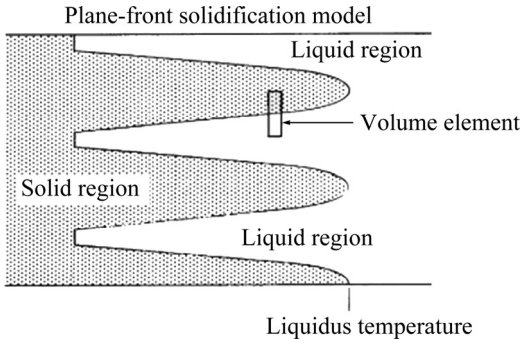

Fig. 1 Solidification front with volume element considered in modeling of microsegregation profile

Several analytical models of microsegregation describing the redistribution of the alloying elements during the solidification process are found in Refs. [24−28]. In these models, the analytical treatment of microsegregation is based on the mass balance analysis of the solutes. The simplest formulation is the equilibrium model (Lever rule) which describes the extreme case of the ideal balance between solid and liquid throughout the solidification process. The assumptions used for equilibrium solidification are difficult to obtain under actual industrial conditions. The Lever rule equation can be written in terms of solute concentration and solid fraction [24]:

$$c_{\mathrm{S}}=\frac{k_{\mathrm{eq}}c_0}{[1-(1-k_{\mathrm{eq}})f_{\mathrm{S}}]} \quad (10)$$

where k_{eq} is the equilibrium partition coefficient, c_0 is the initial concentration, c_{S} is the concentration of the solid phase and f_{S} is the solid volume fraction.

For modeling industrial casting processes, the Scheil model is more reasonable. The assumptions of this model are negligible supercooling during solidification, total diffusion of the solute is in the liquid, and there is no diffusion into the solid [26]. This model is different from the Lever rule since it considers that there is no diffusion in the solid and

the solidified solid composition no longer changes. On the other hand, there is a complete mixture in the liquid region. In Scheil model, the solid us and liquidus isotherms are assumed as straight lines, and the solid concentration can be expressed as

$$c_S = k_{eq} c_0 (1 - f_S)^{(k_{eq}-1)} \quad (11)$$

The segregated solute from the solid phase increases the concentration of the liquid until it reaches the concentration of the eutectic. When a fast solidification process occurs, the velocity of the solidification front will not be low enough to allow the homogenization of the liquid and, therefore, a solute-rich layer will be formed in the solidification front. The solute concentration will go through an initial transient and, then, a permanent regime will occur in which the rejection rate of the solute will be equal to the diffusion velocity from the solidification front [29]. It should be emphasized that, since the rejected solute is strongly dependent on the solidification velocity and the solute diffusion is affected by the concentration gradient, it is expected that solute concentration in the formed solid becomes a function of the solidification velocity [27]. Considering the range of solidification velocities observed in the experimental apparatus, more compatible with the industrial environment, modeling assumptions of solid homogenization or even diffusion in the solid are not reasonable.

BURTON et al [22] proposed the inclusion of the solidification front displacement velocity in modeling of the microsegregation profiles, replacing the equilibrium coefficient k_{eq} by effective partition coefficient k_{ef}, which also takes into account the diffusion coefficient of the liquid and the diffusion length scale, and is derived as

$$k_{ef} = \frac{k_{eq}}{k_{eq} + (1 - k_{eq}) \exp\left(\frac{-S_S \delta}{D_L}\right)} \quad (12)$$

where S_S is the solidification speed, δ is the diffusion layer thickness in the liquid phase and D_L is the diffusion coefficient of the liquid phase. The δ depends on the solidification speed (S_S), liquid viscosity and agitation conditions ahead the solid/liquid interface, and its value can vary from 10^{-6} to 10^{-3}m, according to the MEZA et al [6]. The equilibrium partition coefficient (k_{eq}) has been replaced by an effective partition coefficient into the phase-field model through Eq. (5).

4 Experimental

Directional solidification experiment with Al−Cu alloy was conducted at high solidification speeds in a water-cooled solidification system. The experimental cooling curves allowed to determine the thermal parameters, such as cooling rate ($\dot{T}$), solidification speed (S_S) and local solidification time (t_{LS}).

An optical microscope was used to produce digital images that were analyzed using Goitaca image processing software in order to measure the tertiary dendritic arm spacing (λ_3).

The measurements of microsegregation profiles were taken with a scanning electron microscope JEOL for different cooling rates ($\dot{T}$) and positions along casting length.

Directional solidification has been widely used to produce uniform structures and to allow better control of the solidification [1,3,6,30]. In this work, a unidirectional solidification apparatus is adopted, of which heat is extracted from bottom of the mold by water cooling system, as shown in Fig. 2.

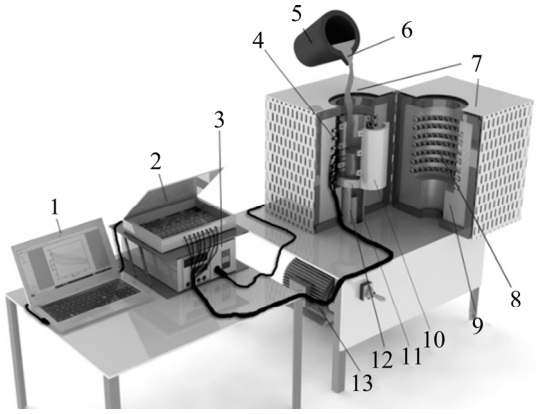

Fig. 2 Diagrammatic representation of equipment: 1—Personal computer and data acquisition software; 2—Data logger hardware; 3—Temperature controller system; 4—Type K thermocouples; 5—Crucible; 6—Melt; 7—Unidirectional solidification furnace; 8—Electric heaters; 9—Ceramic fiber insulation; 10—Steel mold; 11—Steel plate; 12—Water cooling system; 13—Water pump

The upward solidification system gives better stability in liquid region, since it does not induce convection current during solidification process. In the upward vertical solidification, the solute

concentrations in the mushy zone and in the melt ahead of the dendritic array are expected to be stable because solute enrichment causes an increase in the melt density [31]. The alloy was produced from aluminium (99.9% Al) and copper (99.9% Cu) in a muffle furnace. The chemical composition of the alloy has been measured using an X-ray fluorescence spectrometer.

The temperature mapping during solidification of the Al−5wt.%Cu alloy was made using thermocouples positioned at eight different points located at 5, 10, 15, 20, 35, 45, 60, and 85 mm from the refrigerated base. The cooling rate is experimentally calculated as $\dot{T}=\mathrm{d}T/\mathrm{d}t$, for each measurement point along the casting, at the moment when material reaches the liquidus temperature, and as a general rule, assume that solidification begins at liquidus temperature (T_L) and ends when it reaches the solidus temperature (T_S).

The local solidification time was calculated from time required for a particular position in the casting to solidify once nucleation has begun [31]. The thermocouples are of the “K” type, with stainless steel jacket, 1.3 mm in diameter and protected by two layers of refractory paint. These thermocouples were connected to a high-speed data logger and, therefore, being able to generate the thermal profiles in real time.

The casting with a height of 130 mm was cut for the macrostructural and microstructural analysis. The samples were polished and etched with a 0.5% HF solution during 3 s for micrograph and macrograph analysis [31]. The tertiary dendrite arm spacing (λ_3) was measured on the transverse section by averaging the distance between adjacent side branches. The equation for tertiary dendrite arm spacing, as indicated by ROSA et al [32] is

$$\lambda_3=\frac{L}{n-1} \tag{13}$$

where L is the total spacing from the first to the last tertiary arm, and n represents the number of the existing well developed and parallel dendrite arms in this measuring length L. Dendritic spacing usually refers to the spacing of the primary arms of the dendrites. However, if tertiary arms are present, the spacing will be referred to this one once its smaller dimensions become more significant for the properties of the material, according to BAPTISTA et al [1,30].

The microsegregation measurement initiates at the center of a dendritic arm and ends at the midpoint of the interdendritic region between adjacent arms, defining the microsegregation path by KATTAMIS and FLEMINGS [33], as shown in Fig. 3. About 40 concentration measurements were performed for each examined position along the casting, using a JEOL scanning electron microscope (model JSM5800LV) with a Noran EDS.

Physical properties adopted for this work were

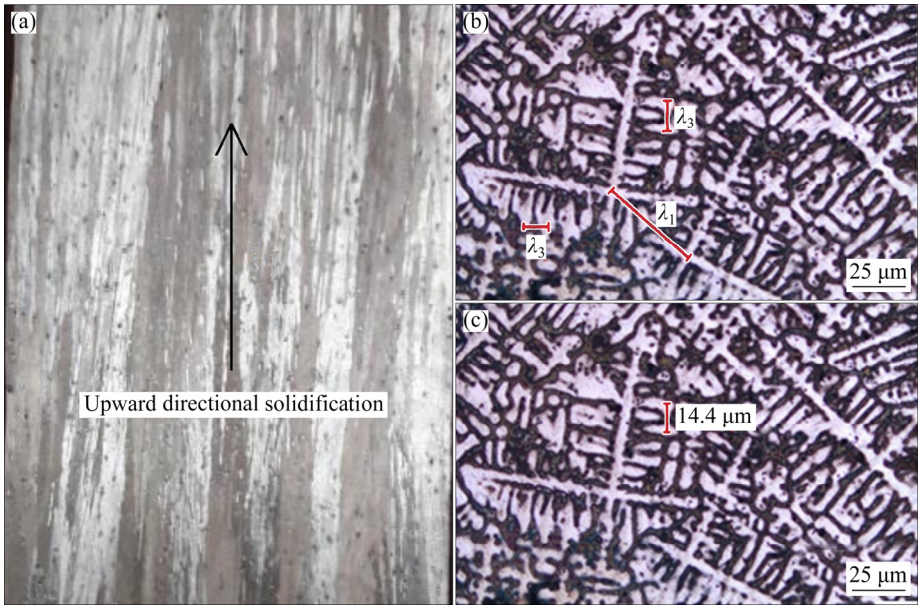

Fig. 3 Directionally solidified ingot: (a) Macrograph of longitudinal sample extracted from ingot; (b) Primary and tertiary dendritic arm spacings of transversal sample; (c) Track considered for measurements of microsegregation profiles

the same used by KOHLER et al [23], KUMOTO et al [34], FERREIRA et al [35] and BEZERRA et al [36], as shown in Table 1.

Table 1 Physical properties of binary Al−5wt.%Cu alloy

Parameter	Value
Liquidus temperature, T_L/K	919.7
Solidus temperature, T_S/K	829.7
Equilibrium partition coefficient, k_{eq}	0.092
Diffusion coefficient in liquid phase, $D_L/(m^2\cdot s^{-1})$	3.6×10^{-9}
Diffusion coefficient in solid phase, $D_S/(m^2\cdot s^{-1})$	3.0×10^{-13}
Slope of liquidus line, $m_e/(K\cdot mol^{-1})$	640
Molar volume, $V_m/(m^3\cdot mol^{-1})$	1.095×10^{-5}
Interface energy, $\sigma/(J\cdot m^{-2})$	0.093
Linear kinetic coefficient, $\mu_k/(m\cdot K^{-1}\cdot s^{-1})$	0.4
Diffusion layer thickness, δ/m	4.4×10^{-6}

5 Results and discussion

5.1 Experimental cooling curves and as-cast microstructure of binary Al−5wt.%Cu alloy

Figure 4 shows the phase diagram of the Al−Cu system calculated by Thermo-Calc software using the aluminum database v.4.0. For Al−5wt.%Cu alloy, in cooling process the solidification begins at liquidus temperature of 646.7 °C and ends when the temperature reaches its solidus temperature of 556.7 °C, as indicated in Fig. 4(a), highlighting the liquid−solid transformation region.

It is worth mentioning that solidification interval is determined by the difference of liquidus and solidus temperatures ($\Delta T_S=T_L-T_S$) and as-cast alloys with wide solidification interval make them susceptible to segregation during the solidification process. In the solidification experiments focused on segregation phenomenon, the equilibrium partition coefficient is usually determined considering data from the equilibrium phase diagram. In the present work, k_{eq}=0.092 corresponds to the concentration ratio between solid (c_S=0.46 wt.% Cu) and liquid (c_L=5 wt.% Cu).

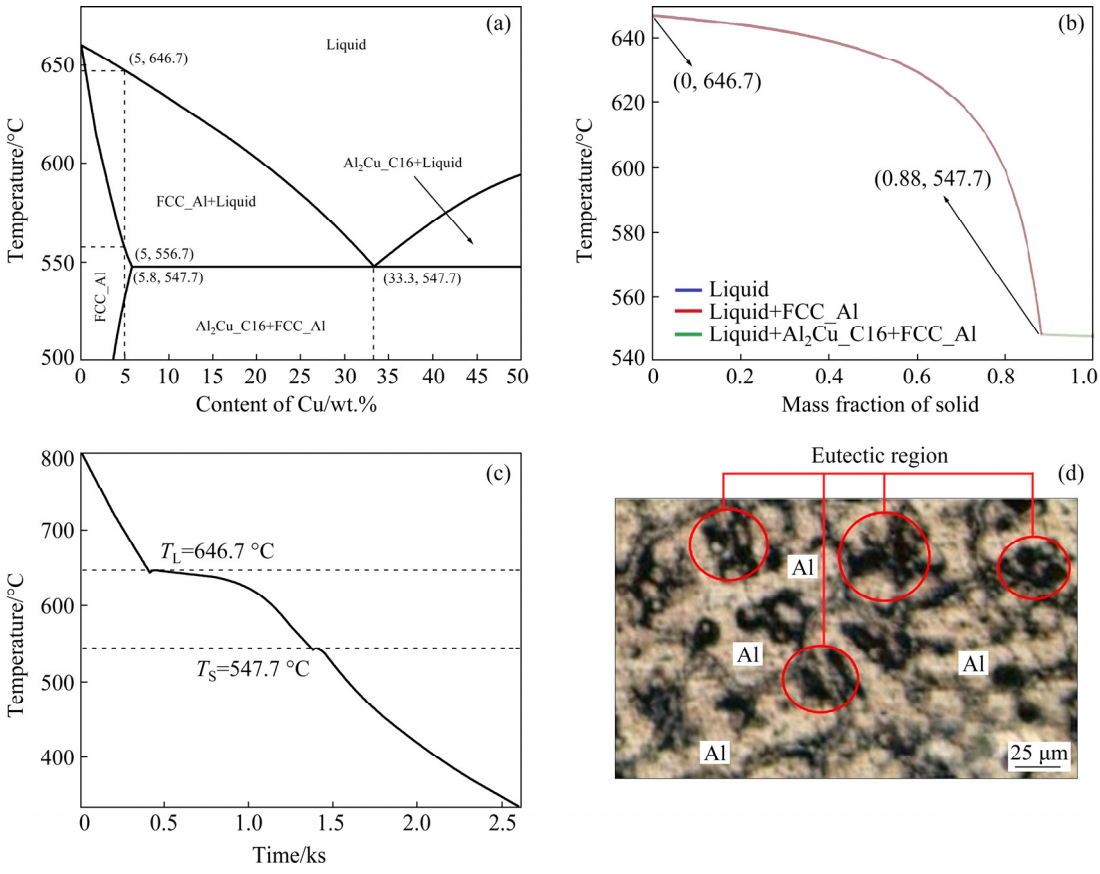

Fig. 4 Phase diagram of Al−5wt.%Cu alloy simulated by Thermo-Calc software with aluminum database v.4.0 (a), equilibrium Scheil model revealing precipitation of phases during cooling (b), experimental cooling curve under slow cooling rate (c), and as-cast microstructure of binary Al−5wt.%Cu alloy (d)

Hypereutectic and hypoeutectic regions are shown in Fig. 4(a) where the limit of copper solubility in solid phase can be found at 5.8 wt.% Cu with T=547.7 °C. Figure 4(b) shows Scheil simulations and the corresponding experimental validation for the examined alloy. Through the graph of temperature versus solid fraction, one can predict the growth sequence of each phase from the liquid region during cooling process. For the considered alloy, at 646.7 °C the FCC_Al phase starts to grow as the primary phase, and at 547.7 °C all the solute-enriched liquid will give rise a 12% eutectic fraction. Figure 4(c) was obtained under a slow cooling condition from the melt, with 300 g of metal, at a cooling rate of about 0.35 °C/s. This cooling curve experimentally obtained shows the temperatures of transformation and corroborated with those predicted by the Scheil model. The dendritic microstructure along the casting length is shown in Fig. 5. Figure 5(a) shows the macrograph of the as-cast ingot, which evidences the columnar and equiaxed structures found after solidification experiment. The length of columnar structure is about 120 mm from the water-cooled bottom, which is favored by directional heat extraction during the experiment. In this position (120 mm), one can see columnar to equiaxed transition (CET) and above this transition an equiaxed zone is predominant. The dendritic microstructures obtained with different solidification speeds (S_S) and cooling rates ($\dot{T}$) are shown in Figs. 5(b−e), the in which information about position (P), values of tertiary dendrite arm spacings (λ_3), solidification speed (S_S) and cooling rate ($\dot{T}$) can be found. Very fine to large dendritic structures can be observed in these figures; the changes found in the size of microstructure are due

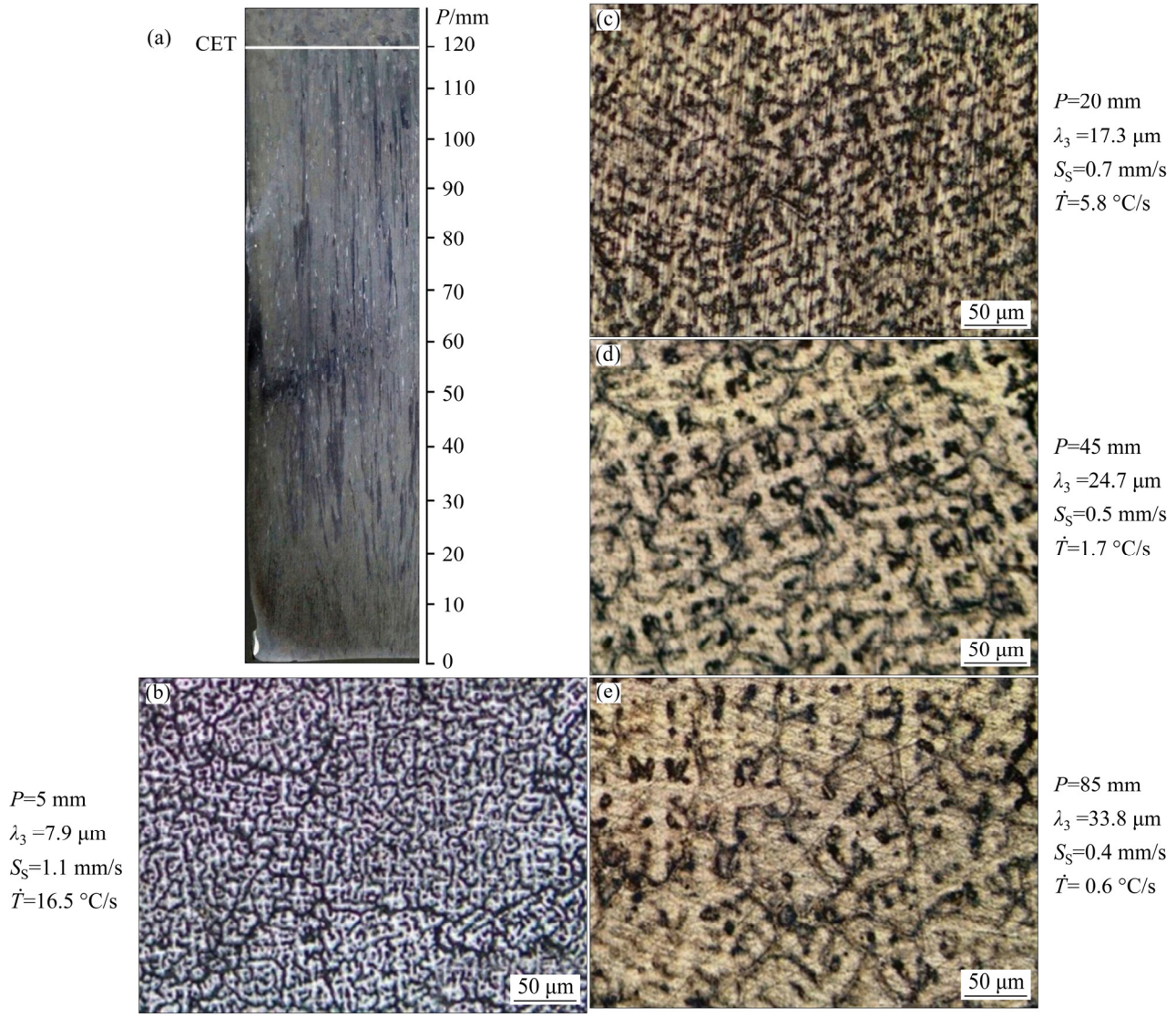

Fig. 5 Macrograph (a) and micrographs (b−e) of samples from transverse sections along casting length

to the wide range of cooling rate and solidification speed observed during the upward directional solidification. The directional solidification assemblies with water-cooled molds are useful when high cooling rates are intended to be achieved. According to SALES et al [31], the thermal parameter that exerts the highest influence on the mechanical properties is the cooling rate, as the microstructure of the material is refined when solidification proceeds at a high rate. A further advantage of microstructural refining, when dealing with aluminum alloys susceptible to heat treatment, is the enhancement in their mechanical properties; as particles formed during solidification will be smaller and will require less time to dissolve during heat treatment. The images shown in Figs. 5(b−e) allow appreciating how λ_3 and the size of Al_2Cu particles are refined as the distance to the mold bottom is reduced. At room temperature, the microstructure consists of primary dendrites (Al-rich) surrounded by a finely divided eutectic mixture of two solid phases FCC_Al+Al_2Cu (Cu-rich). The primary dendrite is represented by a surface with a whitish appearance, while the FCC_Al+Al_2Cu is represented by stained surface with darkened appearance.

5.2 Effect of position on thermal variables and dendritic arm spacing

From the cooling curves determined during the solidification experiment, the position of liquidus temperature as a function of time can be found. The derivative of position of liquidus temperature as a function of time, permits that the solidification speed as a function of time can be determined. Through the experimental equations (P and S_S) as shown in Table 2, it is possible to obtain an equation for the solidification speed (S_S) as a function of position. In this work, the equations are briefly summarized in Table 2, readers can refer to Refs. [1,30,31] for more details of the formulation.

Table 2 Experimental equations showing relationship between position of liquidus temperature P and time t, solidification speed S_S and time t, and solidification speed S_S and position of liquidus temperature P

Position of liquidus temperature as function of time	Solidification speed as function of time	Solidification speed as function of position
$P=2.1t^{0.72}$	$S_S=1.5t^{-0.28}$	$S_S=2.1P^{-0.38}$

Next, the relationships between thermal parameters (solidification speed and local solidification time) with position along the length of the casting are shown in Fig. 6. Comparatively analyzing the profiles of the solidification speed (S_S) and local solidification time (t_{LS}) versus position (P), it can be observed that S_S is seen to decrease faster at the position close to the mold bottom, followed by a gradual decrease with position in the casting. However, the local solidification time increases with position along the casting length. This behavior of local solidification time is because a high solidification speed favors a rapid solidification. The solidification time, in turn, affects the morphology of microstructure, such as grain size and dendritic arm spacing.

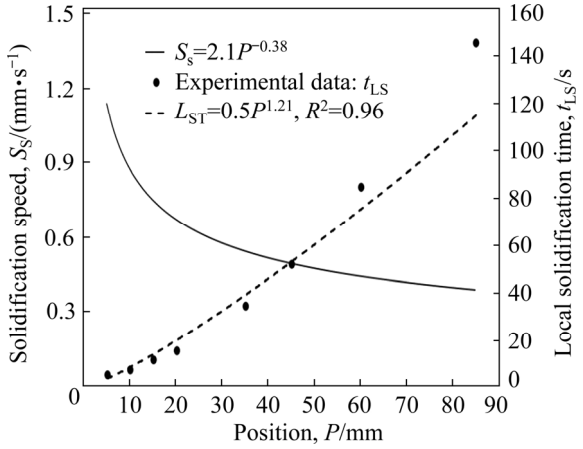

Fig. 6 Solidification speed (S_S) and local solidification time (t_{LS}) versus position (P)

Figure 7 shows variations of the cooling rate and tertiary dendrite arm spacing along the casting length. It can be observed in Fig. 7 that cooling rate decreases with position, which is evidenced by experimental law ($\dot{T}=169.3P^{-1.2}$). This profile is because the water-cooling system favors higher cooling rate in the region close to the mold bottom, which decreases along the casting length because of the increase in thermal resistance of the solidified layer. The cooling rate has been determined considering the temperature versus time data immediately after the passage of the liquidus temperature for each position. The temperature data were collected at intervals of 0.001 s, in order to find an accurate determination of the cooling rate. The cooling rate and solidification speed related to the position are aspects acting in parallel during the

solidification experiment, which adjust the changes of the size and morphology in microstructure of as-cast alloy. As the solidification process proceeds, the continuous increase of the tertiary dendrite arm spacing along the casting length can be observed in Fig. 7.

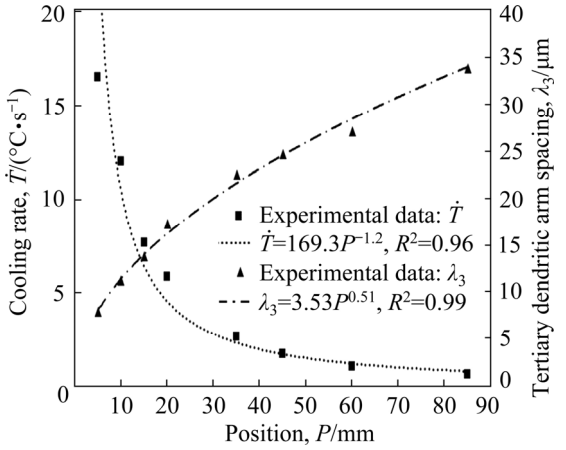

Fig. 7 Cooling rate ($\dot{T}$) and tertiary dendrite arm spacing (λ_3) versus position (P)

5.3 Effect of solidification speed on microsegregation and effective partition coefficient

Considering that solidification experiment of aluminium alloy has been carried out under non-equilibrium conditions, it is necessary to monitor the microsegregation profiles in high solidification speed. To understand the microsegregation phenomenon, the microsegregation profiles were experimentally measured along the casting length. Figure 8 depicts the experimentally measured microsegregation profiles along the microsegregation path, taken from the center of a tertiary dendritic arm (P=0) to the center of the interdendritic region (P=λ_3/2), considering adjacent tertiary dendritic branches. Microsegregation profiles move upward with the increase in solidification speed, which indicates that solubility of copper solute increases with the increase in solidification speed. This is in agreement with the effect of solidification speed on microsegregation on Al alloys reported in previous studies [6,30,37].

Mathematical models using equilibrium partition coefficient (k_{eq}), may not adequately describe the solidification phenomenon. In order to improve the prediction capability of phase-field model adopted in present work, the effective partition coefficient (k_{ef}) was experimentally determined. Equation (10) has been used to create a plot of k_{ef} versus S_S. In order to determine an experimental equation of k_{ef} as a function of S_S, a curve fitting technique has been adopted on points, as shown in Fig. 9.

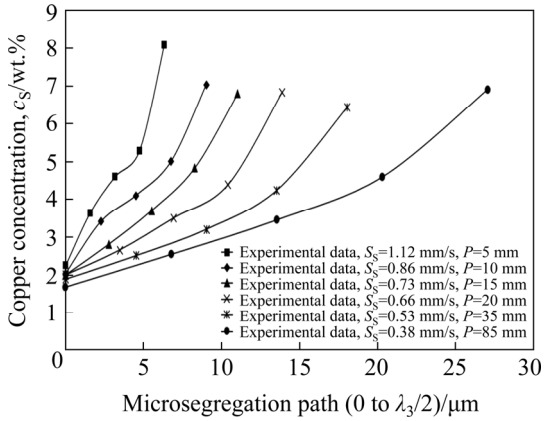

Fig. 8 Effect of solidification speed (S_S) on microsegregation profile at different positions (P) along casting length

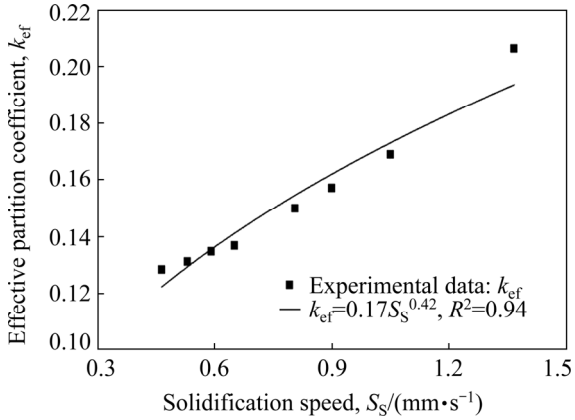

Fig. 9 Effective partition coefficient (k_{ef}) as function of solidification speed (S_S)

In this work, the numerical results calculated by phase-field model were obtained by disregarding the equilibrium partition coefficient (k_{eq}) and, instead, a k_{ef} as a function of S_S, was considered during simulations. The comparison between experimental microsegregation profiles and those predicted by the phase-field model using k_{ef} are shown in Fig. 10.

We compared the calculated results of one-dimensional phase-field with the experimental results in different positions and for a range of solidification speed experimentally examined. The parameters used in the phase-field model, obtained from physical properties of the alloy, Table 1, were

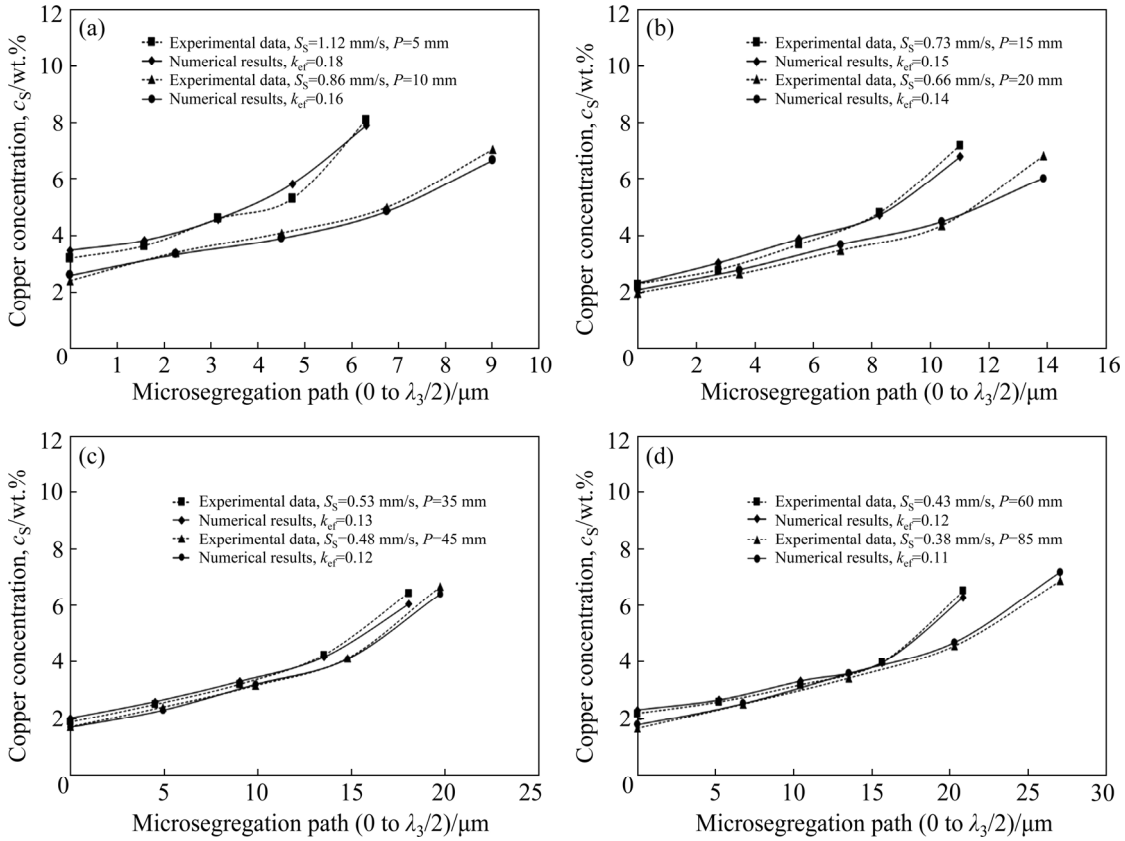

Fig. 10 Comparison of microsegregation profiles between numerical results calculated via phase-field model and experimental data

derived from Eqs. (3)−(6). The boundary condition adopted during calculations is a zero-flux condition. In the calculations, the system temperature is uniform and continuously decreases with cooling rate from the initial temperature (T_0), which is slightly lower than the liquidus temperature of the Al−5wt.%Cu alloy. The excellent agreement between results shown in Fig. 10 is because cooling rates (Fig. 7) were experimentally determined, effective partition coefficient (Fig. 9) was calculated as a function of solidification speed and besides that the phase-field model is able to calculate the back-diffusion during the simulations.

5.4 Solidification speed and dendritic arm spacing determined experimentally and predicted by phase-field model

Using the experimental cooling rate and effective partition coefficient in phase-field model, others numerical results were obtained as follows. Figure 11 exhibits the results of the solidification speed as a function of time obtained from experimental data and predicted by phase-field model.

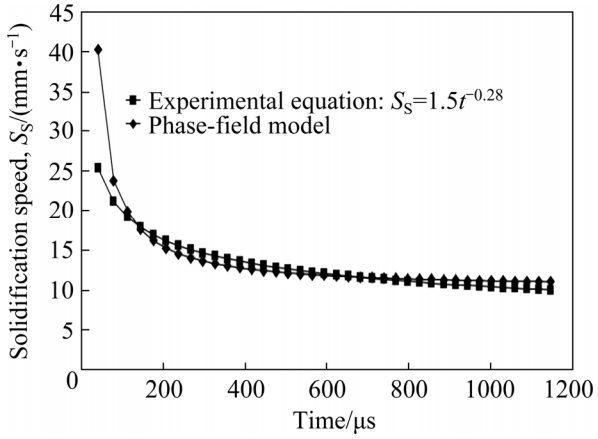

Fig. 11 Solidification speed (S_S) determined experimentally and predicted by phase-field model

Results in Fig. 11 display good agreement between the solidification speeds predicted by phase-field model and the experimentally determined results. But, as expected, the behavior is clearly nonlinear, with both curves tending downwards as the solidification process proceeds. In Fig. 11, the speed is seen to decrease faster at the onset of solidification, in both cases considered. This rate then gradually dwindles toward

completion of the solidification process. The reduction in interface mobility is due to zero-flux condition considered in calculations and the solute segregation from solid region to liquid region during the solidification. In the present calculation, interface motion is determined from the driving force, represented by the third term on the right hand in Eq. (1).

The focus of next simulations, Fig. 12, is on the tertiary dendrite arm spacing predicted by phase-field for different positions along the casting length. In this calculation, we compared the results of a two-dimensional phase-field simulation with the data found in solidification experiment, and a good agreement can be observed between them. In both curves, the tertiary dendrite arm spacing increases with the increase of position. It is worth noting that with water-cooled system used during experiment, high cooling rates were found in regions close to the mold bottom. These high cooling rates, in turn, are responsible for the refinement effect on the dendritic microstructure. In preparing these simulations, we paid appreciable attention to the choice of a suitable computational grid. Even not too sharp interface grid may still be fine enough to capture correctly the phenomena that occur in solidification process. Thus, a sufficiently large number of nodal points around the interface should be obtained so that phase-field gradients can be captured, for it is these gradients that define the phase and concentration fields. In order to do that, a square mesh (dimensions: $\Delta x=\Delta y=1.5\times10^{-7}$ m) has been used when the time step equals 1.7×10^{-6} s.

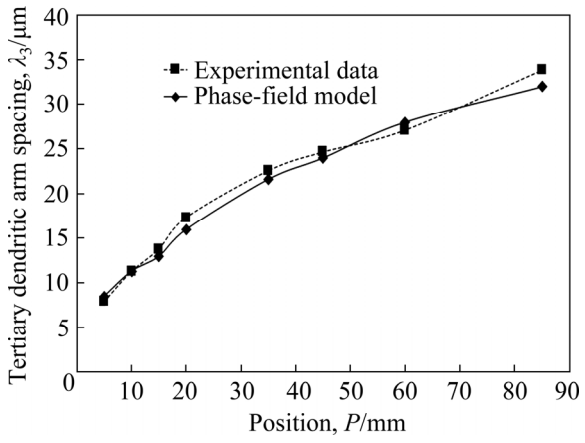

Fig. 12 Tertiary dendrite arm spacing (λ_3) predicted by phase-field model and experimentally obtained after solidification

5.5 Dendrite morphology, solute concentration and phase-field variable

Figure 13 shows the dendritic morphology of Al−5wt.%Cu alloy calculated by phase-field model. In Fig. 13, the dendrite starts to grow from the center of computational domain to the corners of the domain. One of the interesting phenomena is the asymmetry in the side branching found in the dendritic arms. Such asymmetry is related to the concentration distribution and a noise term on the right side of phase-field equation of Eq. (1).

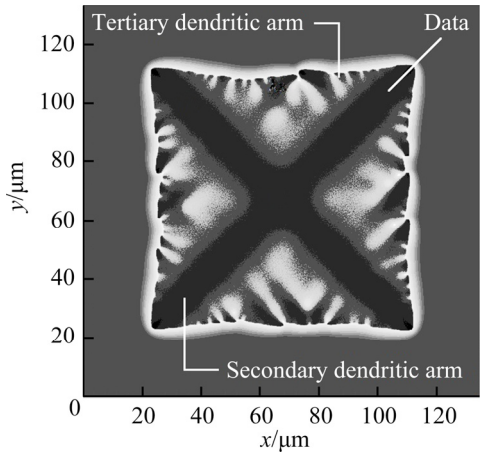

Fig. 13 Dendritic morphology calculated by phase-field model

Figure 14 shows concentration profile of copper and the phase-field variable across the interface at the dendrite tip, as indicated in Fig. 13.

The left vertical axis gives the copper concentration; the right hand one, represents the phase-field variable. ϕ=1 represents the solid phase, whereas ϕ=0 is the liquid. The solid/liquid interface lies between ϕ=1 and 0. Therefore, one can see that

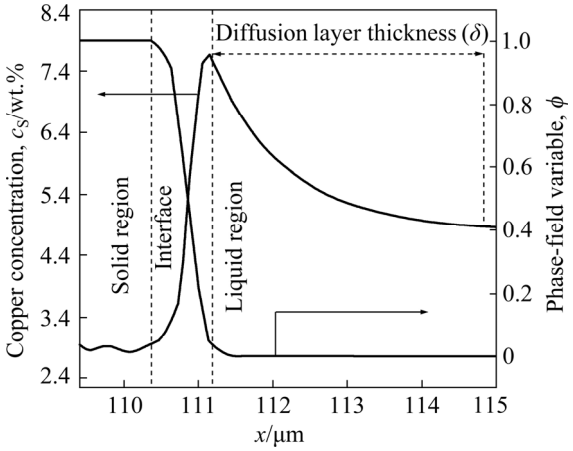

Fig. 14 Copper concentration profile and phase-field variable across solid/liquid interface

solid region is very poor in copper. This is because, during simulation of solidification, the copper solute is rejected into the liquid phase, which then becomes rich in copper just ahead of the solid/liquid interface. In Fig. 14, as we move farther to the right, hence away from the interface, i.e., right after concentration peak, copper concentration decreases exponentially, towards its initial value in the liquid. This behavior occurs within the thickness of the diffuse layer (δ). Such tendency seems to be in agreement with the consideration that the Gibbs free energy is more negative in the solid phase, as discussed by FERREIRA and OLIVÉ [14]. As for the seeming coincidence in the peak between concentration curves and phase-field variable, this merely stems from the fact that the concentration axis, to the left, features a scale of magnitude higher than that for the phase-field variable, to the right.

6 Conclusions

(1) The solidification experiment results of Al−5wt.%Cu alloy show that a quite complex dendritic arrangement prevailed along the entire length of casting, giving rise to tertiary dendrite arms.

(2) The thermal variables such as solidification speed and local solidification time related to the positions along the casting length, are aspects acting in parallel with cooling rate during solidification process, which conditions the changes of the size in microstructure of as-cast alloy.

(3) The microsegregation curves between adjacent tertiary dendritic arms show that copper concentration increases gradually from the center of tertiary dendritic arm to the center of the interdendritic region. The experimental results show that the copper profiles in the solid region are strongly influenced by the solidification speed, i.e., concentration profiles move upward with the increase of solidification speed.

(4) In order to improve the prediction capability of phase-field model, a new partition coefficient was experimentally determined as a function of solidification speed, during the solidification of binary alloy. Then, phase-field model using the effective partition coefficient and experimental cooling rate was applied to the simulation of microstructure and microsegregation during the solidification of Al−5wt.%Cu alloy.

(5) By performing comparisons between numerical results (microsegregation profiles, solidification speed and dendritic arm spacings) predicted by phase-field model and experimental ones found during solidification experiment, it was found that the computed results by the model showed excellent agreement with experimental data.

(6) This work provides an introduction to the application possibilities of phase-field model. This is a versatile and powerful technique for simulating solidification process. The potential of the phase-field model for applications pertaining to solidification has been demonstrated through the simulations herein.

Acknowledgments

The authors are grateful for FAPERJ (Fundação de Amparo à Pesquisa do Estado do Rio de Janeiro, APQ#1: E-26/010.001942/2019) and CNPq (Conselho Nacional de Desenvolvimento Científico e Tecnológico) for their financial support.

References

[1] BAPTISTA L A S, FERREIRA A F, PARADELA K G, SILVA D M, CASTRO J A. Experimental investigation of ternary Al−Si−Cu alloy solidified with unsteady-state heat flow conditions [J]. Materials Research, 2018, 21: e20170565.

[2] FERREIRA A F, CHRISÓSTIMO W B, SALES R C, GARÇÃO W J L, SOUSA N P. Effect of pouring temperature on microstructure and microsegregation of as-cast aluminum alloy [J]. International Journal of Advanced Manufacturing Technology, 2019, 104: 957−965.

[3] GOULART P R, CRUZ K S, SPINELLI J E, FERREIRA I L, CHEUNG N, GARCIA A. Cellular growth during transient directional solidification of hypoeutectic Al−Fe alloys [J]. Journal of Alloys and Compounds, 2009, 470: 589−599.

[4] GÜNDÜZ M, ÇARDILI E. Directional solidification of aluminium–copper alloys [J]. Materials Science and Engineering A, 2002, 327: 167−185.

[5] SILVA A P, GARCIA A, SPINELLI J E. The effects of microstructure and intermetallic phases of directionally solidified Al−Fe alloys on microhardness [J]. Materials Letters, 2012, 89: 291−295.

[6] MEZA E S, BERTELLI F, GOULART P R, CHEUNG N, GARCIA A. The effect of the growth rate on micro-segregation: Experimental investigation in hypoeutectic Al−Fe and Al−Cu alloys directionally solidified [J]. Journal of Alloys and Compounds, 2013, 561: 193−200.

[7] AVAZKONANDEH GHARAVOL M H, HADDAD SABZEVAR M, FREDRIKSSON H. Effect of partition coefficient on microsegregation during solidification of

aluminium alloys [J]. International Journal of Minerals, Metallurgy and Materials, 2014, 21: 980−989.

[8] GÜNDÜZ M, KAYA H, ÇARDILI E, MARASLI N, KESLIOGLU K, SAATÇI B J. Effect of solidification processing parameters on the cellular spacings in the Al−0.1wt%Ti and Al−0.5wt%Ti alloys [J]. Journal of Alloys and Compounds, 2007, 439: 114−127.

[9] MARDARE C C, HASSEL A H. Influence of cooling speed on the solidification of a hyper-eutectic Cu−Sn alloy [J]. Physica Status Solidi A, 2012, 209: 825−831.

[10] ZHAI W, WANG B J, LU X Y, WEI B. Ternary eutectic growth during directional solidification of Ag−Cu−Sb alloy [J]. Applied Physics A, 2015, 121: 273−281.

[11] KAZUHIRO M, TAKAYUKI H, GEN S, OSAMU Y, MINORU K. Effects of Ca addition on solidification structure of Cu−Sn−Zn bronze castings [J]. Materials Transactions, 2007, 48: 799−806.

[12] BATTERSBY S E, COCHRANE R F, MULLIS A M. Microstructural evolution and growth velocity−undercooling relationships in the systems Cu, Cu−O and Cu−Sn at high undercooling [J]. Journal of Materials Science, 2000, 35: 1365−1373.

[13] FERREIRA A F, SILVA A J, CASTRO J A. Simulation of the solidification of pure nickel via the phase-field method [J]. Materials Research, 2006, 9: 349−356.

[14] FERREIRA A F, OLIVÉ L F. Microsegregation in Fe−C−P ternary alloys using a phase-field model [J]. Journal of the Brazilian Society of Mechanical Sciences and Engineering, 2009, 31: 173−180.

[15] WYNBLATT P, LANDA A. Computer simulation of surface segregation in ternary alloys [J]. Computational Materials Science, 1999, 15: 250−263.

[16] SALVINO I M, OLIVÉ L F, FERREIRA A F. Simulation of microsegregation in multicomponent alloys during solidification [J]. Steel Research International, 2012, 83: 723−732.

[17] SALVINO I M, JÁCOME P A D, FERREIRA A F, FERREIRA I L. Analysis of the physical properties of multicomponent alloys on the simulation of solidification by phase-field model [J]. Materials Science Forum, 2012, 730: 703−708.

[18] KIM S G, KIM W T, SUZUKI T. Phase-field model for binary alloys [J]. Physical Review E, 1999, 60: 7186−7197.

[19] WHEELER A A, BOETTINGER W J, MCFADDEN G B. Phase-field model for isothermal phase transitions in binary alloys [J]. Physical Review A, 1992, 45: 7424−7440.

[20] WANG H, GALENKO P K, ZHANG X, KUANG W, LIU F, HERLACH D M. Phase-field modeling of an abrupt disappearance of solute drag in rapid solidification [J]. Acta Materialia, 2015, 90: 282−291.

[21] SOBOLEV S L. Local non-equilibrium diffusion model for solute trapping during rapid solidification [J]. Acta Materialia, 2012, 60: 2711−2718.

[22] BURTON J A, PRIM R C, SLICHTER W P. The distribution of solute in crystals grown from the melt. Part I: Theoretical [J]. The Journal of Chemical Physics, 1953, 21: 1987−1991.

[23] KOHLER F, CAMPANELLA T, NAKANISHI S, RAPPAZ M. Peritectic solidification of Cu−Sn alloys: Microstructural competition at low speed [J]. Acta Materialia, 2008, 56: 1519−1528.

[24] SCHEIL E. Observations on the formation of crystal layer [J]. International Journal of Materials Research, 1942, 34: 70−72.

[25] CLYNE T, KURZ W. Solute redistribution during solidification with rapid solid-state diffusion [J]. Metallurgical and Materials Transactions A, 1981, 12: 965−971.

[26] BRODY H D, FLEMINGS M C. Solute redistribution in dendritic solidification [J]. Transactions of the Metallurgical Society of AIME, 1966, 236: 615−623.

[27] OHNAKA I. Mathematical analysis of solute redistribution during solidification with diffusion in solid phase [J]. Transactions of the Iron and Steel Institute of Japan, 1986, 26: 1045−1051.

[28] KOBAYASHI S. A mathematical model for solute redistribution during dendritic solidification [J]. Transactions of the Iron and Steel Institute of Japan, 1988, 28: 535−542.

[29] DALOZ D, HECHT U, ZOLLINGER J, COMBEAU H, HAZOTTE A, ZALOZNIK M. Microsegregation, macrosegregation and related phase transformations in TiAl alloys [J]. Intermetallics, 2011, 19: 749−756.

[30] BAPTISTA L A S, PARADELA K G, FERREIRA I L, GARCIA A, FERREIRA A F. Experimental study of the evolution of tertiary dendritic arms and microsegregation in directionally solidified Al−Si−Cu alloys castings [J]. Journal of Materials Research and Technology, 2018, 8: 1515−1521.

[31] SALES R C, JUNIOR P F, PARADELA K G, GARÇÃO W J L, FERREIRA A F. Effect of solidification processing parameters and silicon content on the dendritic spacing and hardness in hypoeutectic Al−Si alloys [J]. Materials Research, 2018, 21: e20180333.

[32] ROSA D M, SPINELLI J E, FERREIRA I L, GARCIA A. Cellular/dendritic transition and microstructure evolution during transient directional solidification of Pb−Sb alloys [J]. Metallurgical and Materials Transactions A, 2008, 39: 2161−2174.

[33] KATTAMIS T Z, FLEMINGS M C. Dendrite morphology, microsegregation and homogenization of low-alloy steel [J]. Transactions of the Metallurgical Society of AIME, 1965, 223: 992−999.

[34] KUMOTO E A, ALHADEFF R O, MARTORANO M A. Microsegregation and dendrite arm coarsening in tin bronze [J]. Journal of Materials Science & Technology, 2002, 18: 1001−1006.

[35] FERREIRA A F, PARADELA K G, JUNIOR P F, GARCIA A. Phase-field simulation of microsegregation and dendritic growth during solidification of hypoeutectic Al−Cu alloys [J]. Materials Research, 2017, 20: 423−429.

[36] BEZERRA B N, SACRAMENTO D J, FERREIRA A F, GARCIA A, FERREIRA I L. Application of a phase-field model to multicomponent Al−Cu−Si alloys [J]. Materials Research, 2020, 23: e20200198.

[37] KHAN M I, MOSTAFA A O, ALJARRAH M, ESSADIQI E, MEDRAJ M. Influence of cooling rate on microsegregation behavior of magnesium alloys [J]. Journal of Materials, 2014, 2014: 1−18.

定向凝固亚共晶 Al−Cu 合金显微组织演化和显微偏析：实验数据和相场模拟结果比较

Alexandre F. FERREIRA[1], Ivaldo L. FERREIRA[2], Rangel P. ALMEIDA[1],
José A. CASTRO[1], Roberto C. SALES[1], Zilmar A. JUNIOR[1]

1. Graduate Program on Metallurgical Engineering,
Federal Fluminense University, 27255-125, Volta Redonda, RJ, Brazil;
2. Federal University of Pará, College of Mechanical Engineering, 66075-110, Belém, PA, Brazil

摘　要：利用相场模型预测 Al−Cu 合金的显微偏析、凝固速度、枝晶臂间距和枝晶形貌，并将模拟结果与实验结果进行比较。计算中采用冷却速率和有效分配系数的实验值。相场模拟的显微偏析结果与实验值吻合良好，这是由于模型中考虑冷却速率、有效分配系数和溶质的反扩散。凝固速度的计算结果与实验结果吻合较好。将通过相场模型计算的三次枝晶臂间距与实验数据进行比较，两者吻合较好。由于高冷却速率对显微组织的细化作用，枝晶臂间距随位置增大而增大。最后，通过二维模拟得到与实验结果相似的枝晶形貌。

关键词：亚共晶 Al−Cu 合金；有效分配系数；枝晶臂间距； 显微偏析；相场模型

(Edited by Wei-ping CHEN)